Operando Interaction and Transformation of Metastable Defects in Layered Oxides for Na-Ion Batteries

Oleg Yu. Gorobtsov,* Hayley Hirsh, Minghao Zhang, Dina Sheyfer,
Long Hoang Bao Nguyen, Stephanie D. Matson, Daniel Weinstock, Ryan Bouck,
Ziyi Wang, Wonsuk Cha, Jörg Maser, Ross Harder, Ying Shirley Meng, and Andrej Singer

Non-equilibrium defects often dictate the macroscopic properties of materials. They largely define the reversibility and kinetics of processes in intercalation hosts in rechargeable batteries. Recently, imaging methods have demonstrated that transient dislocations briefly appear in intercalation hosts during ion diffusion. Despite new discoveries, the understanding of impact, formation and self-healing mechanisms of transient defects, including and beyond dislocations, is lacking. Here, operando X-ray Bragg Coherent Diffractive Imaging (BCDI) and diffraction peak analysis capture the stages of formation of a unique metastable domain boundary, defect self-healing, and resolve the local impact of defects on ionic diffusion in $Na_xNi_{1-y}Mn_yO_2$ intercalation hosts in a charging sodium-ion battery. Results, applicable to a wide range of layered intercalation materials due to the shared nature of framework layers, elucidate new dynamics of transient defects and their connection to macroscopic properties, and suggest how to control the nanostructure dynamics.

1. Introduction

In materials science, "transistor electronics exist because of the controlled presence of imperfections in otherwise nearly perfect crystals".[1] Point defects are equilibrium effects that enable sophisticated control routes of electronic properties. High-dimensional crystal defects—dislocations and domain boundaries—are intrinsically non-equilibrium phenomena, making them more challenging to understand and control than point defects. Nevertheless, developing successful models for dislocation nucleation, migration, and interaction has transformed the understanding of plasticity and diffusion in metals.[2] While high-dimensional defects are rare in bulk ceramic crystals due to their high Peierls stress,[2] recent research has revealed a possible abundance of dislocations[3–6] and domain boundaries[7–9] in nano-sized ceramics. In layered oxides for lithium- and sodium-ion batteries (respectively LIBs and SIBs from here on), drastic structural rearrangements during cycling can induce the formation of defects, which can impede or facilitate the ionic diffusion process[9,10] and strongly affect the electrochemical performance of the cell, leading to capacity fading.[3] In SIBs—a rapidly evolving safe,[11] sustainable, and inexpensive energy storage solution for large-scale applications[12]—the cathode materials display particularly drastic structural rearrangements, which may negatively affect the durability through defect formation.[13,14]

Battery cathodes are complex ceramics-polymer-carbon composites. Understanding the mechanisms behind defect formation and dynamics in materials comprising multicomponent devices requires operando measurements of structural processes. The primary challenges for obtaining insightful information on the thermodynamics and kinetics lie in resolving defects at the nanoscale in the electrochemically active material during operation, and in precisely measuring the defect orientation in 3D, which is required in layered materials due to their anisotropy. Most conventional in situ and operando techniques applied to battery materials,[15] independently of the probe used, fail to satisfy all requirements simultaneously. The multitude of traditional X-ray diffraction and absorption methods that allow operando and in situ measurements[15] do not directly image defects in nanomaterials. In situ electron microscopy[16] allows a direct 2D visualization of dislocations but is challenging to perform operando in multicomponent devices due to the absorption and

O. Y. Gorobtsov, S. D. Matson, D. Weinstock, R. Bouck, Z. Wang,
A. Singer
Department of Materials Science and Engineering
Cornell University
Ithaca, NY 14853, USA
E-mail: gorobtsov@cornell.edu
H. Hirsh, M. Zhang, L. H. B. Nguyen, Y. S. Meng
Department of NanoEngineering
University of California
San Diego, La Jolla, CA 92093, USA
D. Sheyfer, W. Cha, J. Maser, R. Harder
Advanced Photon Source
Argonne National Laboratory
Argonne, IL 60439, USA
Y. S. Meng
Pritzker School of Molecular Engineering
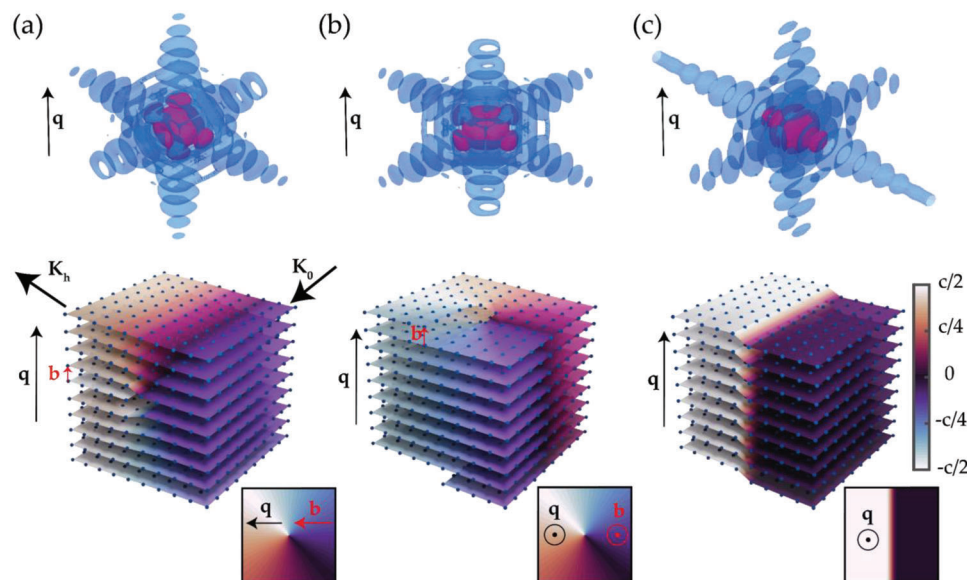The University of Chicago
Chicago, IL 60637, USA

Figure 1. Operando Bragg Coherent Diffractive Imaging (BCDI). Crystal defects (edge dislocation (a), screw dislocation (b), antiphase domain boundary (c)) generate characteristic 3D reciprocal space patterns (top) in coherent X-ray scattering. The phase retrieval algorithm allows inversion of the diffraction profiles into 3D electron density and atomic displacements of the scattering planes (bottom). Here K_0, K_h, q are the incident and scattered wavevectors and a scattering vector respectively, c is the lattice constant perpendicular to the layers. An analysis of the dimensionality and orientation of the singularities in atomic displacements allows identification of the type of defect.

radiation sensitivity of the battery components. Operando optical methods[17] do not reach sufficient resolution. Operando neutron scattering[18] does not provide nanoscale resolution or direct defect imaging. To overcome these challenges, synchrotron-based operando X-ray Bragg Coherent Diffractive Imaging (BCDI)[3,19] (Experimental Section, Figure S6, Supporting Information) has been developed. Operando BCDI generally combines three critical advantages over traditional characterization techniques, making it a suitable tool to investigate defects under dynamic conditions: 1) coherent diffraction captures the 3D distribution of lattice displacement and atomic defect configuration with 10 nm resolution within individual nanoparticles; 2) X-ray penetration depth enables measurements during electrochemical cycling in a fully operational battery; and 3) high X-ray flux allows capturing phenomena with a few-minute time resolution.

Operando BCDI has demonstrated sufficient resolution to detect transient dislocations in LIB cathode materials.[3,19] Nevertheless, beyond the demonstration of existence, the mechanisms of transient defect evolution in cathode materials during operation remain largely unstudied. The local impact of the defects on the material properties was thought to be beyond the operando methods resolution. Defects directly observed previously with BCDI include dislocations and dislocation loops[20] with a Burgers vector b component along the scattering vector q. These defects produce recognizable vortices in reconstructed displacement maps (**Figure 1**a,b).[19,21] The direction of b determines the type of the observed dislocation: either perpendicular (edge, Figure 1a) or parallel (screw, Figure 1b) to the dislocation line. Observable planar defects, such as antiphase/out-of-phase domain boundaries, generate a lattice displacement in the domain volume in the direction of the momentum transfer q (Figure 1c), while stacking faults in atomic crystals can generate a

2D-manifold of increased strain. Measuring multiple Bragg reflections can be used to image twin domains.[22]

Here, we have applied operando BCDI and diffraction peak analysis to $Na_xNi_{1-y}Mn_yO_2$ intercalation hosts in a charging sodium-ion battery to capture the stages of formation of a unique metastable domain boundary, observe defect self-healing and resolve the impact of defects on local ionic diffusion. Our operando real-space nanoimaging demonstrates dynamic interaction of metastable defects in sodium-ion intercalation hosts, elucidates differences in defect formation between sodium-ion and lithium-ion battery layered oxides, and opens potential access to direct studies of local effects of structural defects and their application for nanoengineering in battery materials. We have investigated several cathode grains in three cells and two materials. The first section of the paper addresses and explains BCDI results on the example of a particular grain in P2-$Na_{0.78}Ni_{0.23}Mn_{0.69}O_2$ in which we tracked the boundary and defect self-healing. The second section addresses the statistical results of BCDI measurements over multiple grains in several cells with P2-$Na_{0.78}Ni_{0.23}Mn_{0.69}O_2$ and P2-$Na_{0.66}Ni_{0.33}Mn_{0.66}O_2$.

2. Results and Discussion

2.1. Operando Defect Formation and Interaction Imaging in P2-$Na_{0.78}Ni_{0.23}Mn_{0.69}O_2$

In this study, we tracked the structural evolution in the sodium transition metal oxide (TMO) cathode within constituent grains of two compositions, P2-$Na_{0.78}Ni_{0.23}Mn_{0.69}O_2$[23] and P2-$Na_{0.66}Ni_{0.33}Mn_{0.66}O_2$.[24,34] The two systems, P2-$Na_{0.78}Ni_{0.23}Mn_{0.69}O_2$ and P2-$Na_{0.66}Ni_{0.33}Mn_{0.66}O_2$, exhibit different Ni–Mn and Na^+-vacancy orderings, which have a

ADVANCED
SCIENCE NEWS

www.advancedsciencenews.com

ADVANCED
ENERGY
MATERIALS

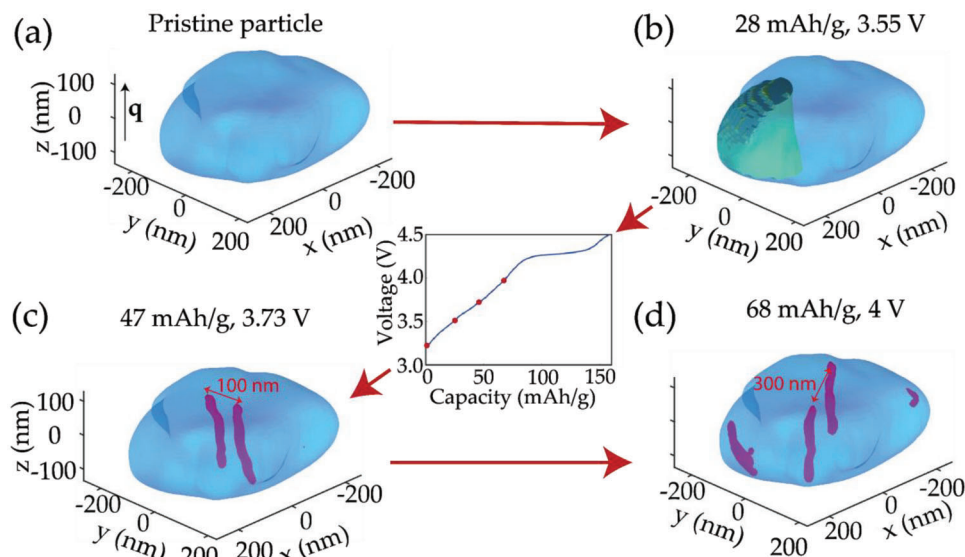www.advenergymat.de

Figure 2. Operando Bragg Coherent Diffractive Imaging (BCDI). Isosurface rendering (blue transparent) of a P2-Na$_{0.78}$Ni$_{0.23}$Mn$_{0.69}$O$_2$ particle measured during charge. Pristine particle displays no observable defects (a), a domain boundary develops at 3.55 V (b) (green, boundary drawn as isosurface at c/4 displacement level, where c is the unit cell size perpendicular to the layers that includes two TMO layers), two dislocations form (red/magenta lines) at 3.73 V (c), recognized based on Figure 1, and the dislocations move apart at 4 V (d). Electrochemical data is shown in the middle inset, red points mark the X-ray measurements.

direct impact on the structural evolution and electrochemical behavior upon cycling. In P2-Na$_{0.66}$Ni$_{0.33}$Mn$_{0.66}$O$_2$, the electrochemical reaction occurs through a succession of bi-phasic reactions related to a change in the Na$^+$-vacancy at different Na$^+$ contents.[24] On the other hand, P2-Na$_{0.78}$Ni$_{0.23}$Mn$_{0.69}$O$_2$ exhibits a solid solution reaction mechanism, until 4.0 V versus Na$^+$/Na is reached.[23] A comparison between these two systems will help to understand whether the formation of intermediate phases having different Na$^+$-vacancy ordering in bi-phasic reactions will have a direct impact on the formation of dislocations. BCDI provided a time resolution of individual measurements between 1 and 2 min, with an average time step on the order of 30 min between measurements for each particle. Operando X-ray imaging reveals the primary particles of both materials crystallized with a plate-like shape (example for P2-Na$_{0.78}$Ni$_{0.23}$Mn$_{0.69}$O$_2$ in **Figure 2**) and dimensions within 100 nm to 1 µm, which agrees with the ex situ scanning electron microscopy images (SEM) of the material (Note S1, Supporting Information). In a representative particle shown in Figure 2, we observe a dislocation pair (magenta) formation process at a domain boundary (green) during electrochemical desodiation of P2-Na$_{0.78}$Ni$_{0.23}$Mn$_{0.69}$O$_2$. Additional dislocations form along the surface of the grain, as previously observed in Li-ion batteries.[3] The defect signatures are evident in the 2D cross-sections of the displacement within the particle (**Figure 3**). A displacement domain (Figure 3b) with a boundary perpendicular to the layer direction develops (Note S3 and Video S1, Supporting Information) and resolves into two vortices with opposite handedness (Figure 3c; Video S2, Supporting Information). Dislocation lines are parallel to the scattering vector, q, which is along [002] and perpendicular to the TMO layers. The data reveals continuous displacement vortices with b × q = 2π (where b is the Burgers vector), meaning that b and the dislocation lines are parallel, and the dislocations are

predominantly screw dislocations at the charging stage below 4.2 V.

The BCDI observations allow us to propose a model for the mechanism of the dislocation pair nucleation (Figure 3d–f). First, an out-of-phase domain boundary with a constant displacement difference of c/4 forms, where c is the spacing between two adjacent transition metal-oxide layers. We suggest that the domain boundary collapses to reconnect the layers, creating an antiparallel screw dislocation pair that reaches the particle surfaces, equivalent to a glissile dislocation loop (b in the plane of the loop) (Figure 3f). The exact domain boundary formation and the collapse mechanism likely involve the formation of accompanying partial dislocations,[25] which may be unresolved here due to the limited spatial resolution and the geometry of the X-ray measurement: we only measure displacement along the scattering vector q.[3,19]

We estimate the activation energy E_c for the nucleation of a dislocation pair in pristine conditions in the P2-Na$_{0.78}$Ni$_{0.23}$Mn$_{0.69}$O$_2$ particle as $E_c \approx 1.1 \times 10^{-8} \frac{J}{m}$; the corresponding minimum shear stress assuming homogeneous nucleation would be $\sigma_{zp} \approx$ 80 MPa (Note S2, Supporting Information). If a particle is confined to a fixed volume, the lattice constant change by 0.1% (see **Figure 4**a–d) would result in a stress of 150 MPa by Hooke's law. We expect the soft polymer binder to significantly reduce the external stresses between the particles in the electrode. Therefore, heterogeneous nucleation of dislocation pairs is more likely. Molecular dynamics in Si[26] and diamond[27] and in situ TEM in Pd[28] reported heterogeneous nucleation of dislocations at surfaces which is activated by temperature fluctuations. Our operando data hints at an additional mechanism for heterogeneous dislocation formation: in the intermediate configuration preceding dislocation formation, the boundary reduces the energy barrier and therefore reduces the additional shear stress necessary for creating the dislocation pair.
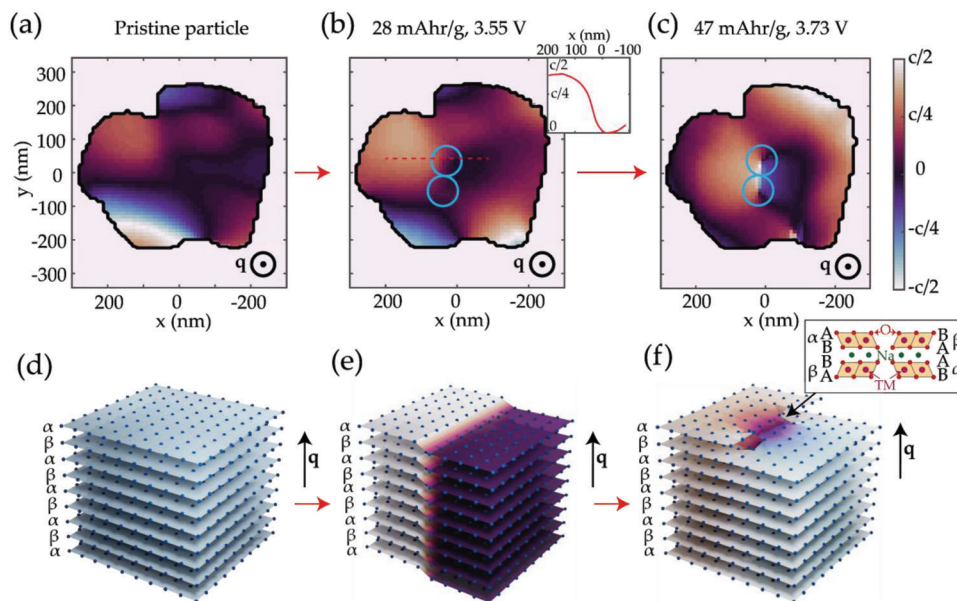
**ADVANCED
SCIENCE NEWS**

www.advancedsciencenews.com

**ADVANCED
ENERGY
MATERIALS**

www.advenergymat.de

Figure 3. Dislocation pair nucleation on a domain border in P2-Na$_{0.78}$Ni$_{0.23}$Mn$_{0.69}$O$_2$. a–c) Comparison of displacement cross-sections at different points during charging (slice through the center of the particle, z = 0, in Figure S5, Supporting Information). Here, the average lattice constant c = 10.836 ± 0.002 Å. Appearance of two screw dislocations (c) on the former domain boundary is visible (blue circles). Inset in (b) shows the displacement along the red dashed line in (b). Dislocations have antiparallel Burgers vectors (left-handed and right-handed screw dislocation). d–f) Schematic representation of a glissile dislocation loop nucleation on the domain boundary. Note the A to B connection of oxygen layers (Delmas's notation) after nucleation (inset, (f)).

The glide force would normally cause oppositely oriented screw dislocations to attract in the absence of external stress.[2] Instead, we find the opposite process: the detected positions of dislocations change with charging to positions closer to the particle surface, meaning that dislocations drift apart (Figure 2) toward the surface of the particle. The dislocation loop expands in the direction of the particle surface (see Figure 4g), and after a 30 mAh g^{-1} change in battery capacity value (2 h at C/10 charge rate), the screw dislocation pair disappears as the lines presumably fully reach the surface (see Figure S8, Supporting Information). The expansion of the loop suggests a continuous external stress perpendicular to the layers over $\sigma_{zp} > 20$ MPa (Note S2, Supporting Information).

In our loop formation model, the dislocation Burgers vector is half of the P2 unit cell constant, c, perpendicular to the layers. Therefore, the oxygen layers reconnect imperfectly (AB slab to BA slab in Delmas' notation) within the loop (Figure 3f, inset), with A to B connection well-known in sodium layered oxides.[29–32] Akin to a stacking fault between a dissociated dislocation in metals, the imperfect connection can introduce additional strain. Indeed, as the battery charges, a planar strain (Figure 4a–d) signature oriented along the [002] direction appears at the position of the dislocation loop (Figure 4f-h). In a separate effect, before the dislocation loop nucleates, we observe a region of relatively lower interlayer distance (a compressive strain of approximately -1×10^{-4}) when the domain boundary is present (Figure 4c,e). We identify two phenomena as the most plausible explanations for a local strain difference near a boundary: 1) coherency strain from the boundary itself;[33] or 2) a relatively higher Na concentration caused by slower Na extraction through the boundary separating the central region, leading to asymmetry in Na concentration.[14]

External stresses could also lead to the observed strain asymmetry. Because the local strain is concentrated in one (central) region, not along the whole domain boundary, the first option does not offer a complete explanation, leaving Na concentration as the more plausible strain origin. The relatively higher Na concentration in the presence of the domain boundary suggests that the boundary likely impedes ion diffusion.

2.2. Generalization and Comparison for Different Grains and Material

We established defect statistics by performing statistical analysis of operando X-ray diffraction data over an ensemble of individual cathode particles[35] (**Figures 5** and **6**). The measured changes in the 3D diffraction intensity around a Bragg peak offer insight into misalignments and phase shifts in individual particles[36] unlike the average obtained in powder X-ray diffraction. Figure 5a shows the typical evolution of a projected diffraction intensity of a P2-Na$_{0.78}$Ni$_{0.23}$Mn$_{0.69}$O$_2$ grain. For most particles, peak broadening along q is limited to 10–20%, while peak width perpendicular to q increases by over 100% (Figure 5b), supporting preferential defect formation perpendicular to the material layers, as such defects would effectively decrease the crystalline correlation length of the structure perpendicular to q (Figure 1). In operando BCDI measurements on P2-Na$_{0.66}$Ni$_{0.33}$Mn$_{0.66}$O$_2$ (Figure 6a,b), as in to P2-Na$_{0.78}$Ni$_{0.23}$Mn$_{0.69}$O$_2$, we have found multiple instances of screw dislocations nucleating perpendicular to the layers and peaks widening perpendicular to q. That is contrary to the expected preferential formation of misfit dislocations between the layers, as the desodiation from
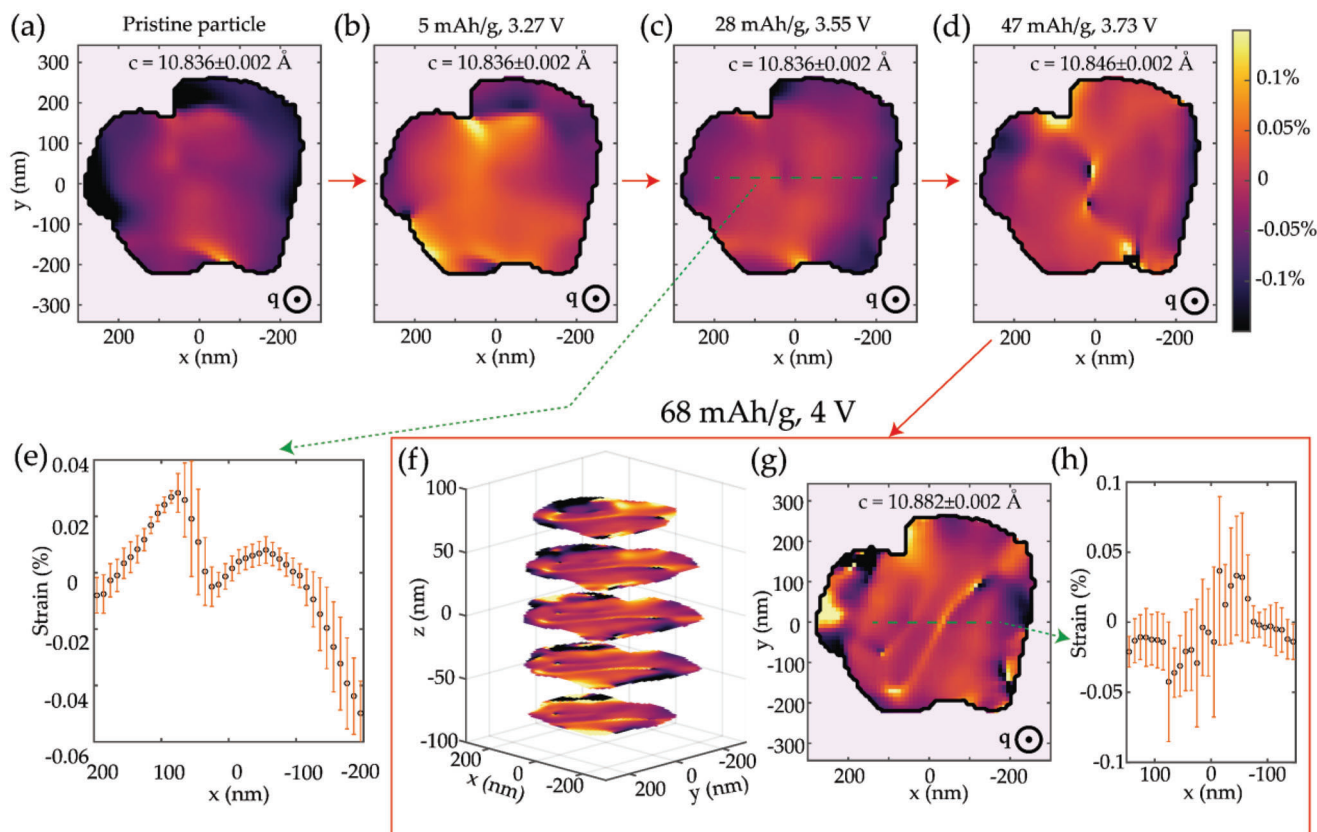
Figure 4. Operando evolution of the strain field inside a single grain. a–d) Cross sections of the strain distribution in a P2-$Na_{0.78}Ni_{0.23}Mn_{0.69}O_2$ crystal particle at different stages of battery charging. Cross sections are through the same plane as in Figure 3, $z = 0$ in Figure 4f (same in Figure S5, Supporting Information). The average lattice constant c is calculated through a center of mass of the Bragg peak, the error is calculated accordingly (the calculated error corresponds approximately to a visible movement of 7 pixels on the detector). e) Linear cross section of the strain, averaged along q, along the green line in (c), showing a 0.02% drop in lattice constant in the particle center. Error is calculated as a standard deviation between repeated phase retrieval results. (f,g) Strain distribution in the particle in the middle of the phase transition, showing a "strain wall" between the dislocations. (h) Cross line of the strain through the "strain wall" at the position shown by green line in (g).

P2-$Na_{0.66}Ni_{0.33}Mn_{0.66}O_2$ occurs through a series of biphasic reactions with the formation of several intermediate phases with differing c-lattice constants, inducing significant stress between the layers and potential delamination.[37] Notably, the Bragg peaks in P2-$Na_{0.66}Ni_{0.33}Mn_{0.66}O_2$ preserve the fringe and speckle structure and higher intensity throughout later stages of charging than in P2-$Na_{0.78}Ni_{0.23}Mn_{0.69}O_2$.

We compared the degree of inhomogeneity in the interlayer distance in both materials by calculating the partial strain energy in the [002] direction (Figures 5c and 6c) from BCDI reconstructions. Strain relative to the average lattice constant of the particle is equivalent to the changes in the lattice constant, making partial strain energy a measure of such inhomogeneity [3]. The energy is calculated as $E_{p,002} = \frac{1}{2}Y_z \int |\varepsilon_{002}(r)|^2 dr$, where Y_z is the Young's modulus along [002] (estimated as 150 GPa[37]), $\varepsilon_{002}(r)$ is the measured strain as in Figure 4a–d, r is the spatial coordinate, and the integration is over the particle volume. The partial strain energy, $E_{p,002}$, in the P2-$Na_{0.78}Ni_{0.23}Mn_{0.69}O_2$ particle in Figures 2–4 (thick solid orange line in Figure 5c) decreases as the domain boundary is formed at 28 mAh g^{-1} and increases again as the boundary resolves into a dislocation pair, supporting the notion that the domain boundary suppresses strain by stor-

ing energy. The strain energy density in both materials is 3–10 times lower in the initial charging stage than in Li containing layered oxides,[3] staying below 0.1–0.2 pJ μm^{-3} during charging. The difference in the strain energy density can be explained by a fast and homogeneous diffusion process of Na^+ thanks to the low activation energy for Na^+ diffusion in the P2-structure[14] and a low charge density of Na^+ compared to Li^+. The specific strain energy in $Na_{0.66}Ni_{0.33}Mn_{0.66}O_2$ up to ≈70 mAh g^{-1} (corresponding to the P2–O2 transition, see Figure S7, Supporting Information) is even lower (2–3 times) than in $Na_{0.78}Ni_{0.23}Mn_{0.69}O_2$, suggesting that the inhomogeneous structural changes are delayed until the P2–O2 transition in $Na_{0.66}Ni_{0.33}Mn_{0.66}O_2$. Even though P2-$Na_{0.66}Ni_{0.33}Mn_{0.66}O_2$ undergoes several bi-phasic reactions during cycling, the formation of intermediate phases with different Na^+-vacancy ordering[24] does not lead to a significant increase in the strain on the particle or the presence of dislocations.

3. Conclusions

Our real-space operando imaging revealed a novel formation mechanism for dislocation loops on the domain boundaries in layered $Na_xNi_{1-y}Mn_yO_2$. The observed lifetime of the dislocation
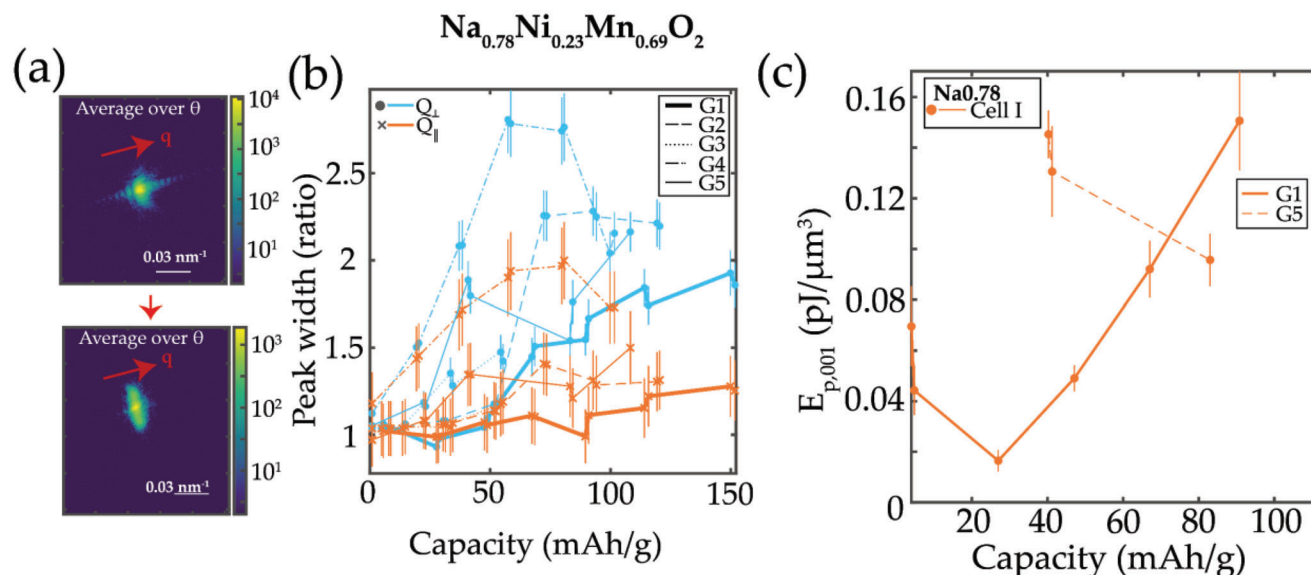
ADVANCED
SCIENCE NEWS

www.advancedsciencenews.com

ADVANCED
ENERGY
MATERIALS

www.advenergymat.de

Figure 5. Expanded analysis over many cathode particles; P2-Na$_{0.78}$Ni$_{0.23}$Mn$_{0.69}$O$_2$. a) Example of evolution of projected (averaged over the reflection angle θ) Bragg peaks for P2-Na$_{0.78}$Ni$_{0.23}$Mn$_{0.69}$O$_2$. Top - pristine, bottom - during charging at 98 mAh g^{-1}. b) Evolution of the peak width for multiple grains, along (x markers, orange) and perpendicular (o markers, blue) to the q direction. Grain shown in previous figures is G1. Error is calculated as an error on width (through kurtosis). c) Specific partial strain energy for some of the particles of P2-Na$_{0.78}$Ni$_{0.23}$Mn$_{0.69}$O$_2$ in the process of charging. Errors are calculated as a standard deviation between strain energy calculated for different particle surface calculated from phase retrieval (10%, 15%, and 20% of the maximum amplitude).
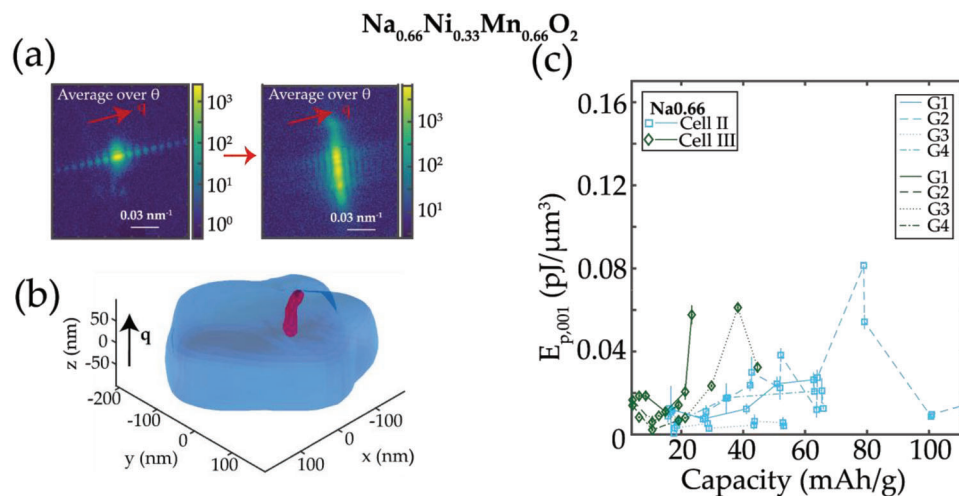

Figure 6. Expanded analysis over many cathode particles; P2-Na$_{0.66}$Ni$_{0.33}$Mn$_{0.66}$O$_2$. a) Example of evolution of projected (averaged over the reflection angle θ) Bragg peaks for P2-Na$_{0.66}$Ni$_{0.33}$Mn$_{0.66}$O$_2$. Left - pristine, right - during charging at 134 mAh g^{-1}. b) Example of a reconstructed particle (blue) with a dislocation (red) for P2-Na$_{0.66}$Ni$_{0.33}$Mn$_{0.66}$O$_2$ at 17 mAh g^{-1}. c) Specific partial strain energy for different particles of P2-Na$_{0.66}$Ni$_{0.33}$Mn$_{0.66}$O$_2$ in different cells in the process of charging. Errors are calculated as a standard deviation between strain energy calculated for different particle surface calculated from phase retrieval (10%, 15%, and 20% of the maximum amplitude).

loop on the order of 30 mAh g^{-1} demonstrates dislocation self-healing during charging and further stresses the importance of operando over ex situ measurements: the latter could miss the presence of transient defects. The operando observation of dislocation formation and self-healing warrants further investigation of the impact of dislocations on the phase transition, possible control of self-healing, and the correlation of microstructure to electrochemistry. Furthermore, the qualitative mechanical model

and the observed planar strain signature within the loop offer a possible mechanism for the formation of stacking fault-type defects often observed ex situ in layered cathode materials[13,39] through improper layer attachment left by the expanding loop. The X-ray observed probable retardation of ion diffusion from the central particle region by the domain boundary contrasts with considerations in Li-ion materials, which suggested that the boundary accelerates ion diffusion.[10,40] It also demonstrates a

new and promising application of BCDI to track ion diffusion in 3D through operando measurements with improved spatial and temporal resolution.

In all particles we reconstructed, for $Na_{0.78}Ni_{0.23}Mn_{0.69}O_2$ and $Na_{0.66}Ni_{0.33}Mn_{0.66}O_2$, we only found screw dislocations and out-of-phase boundaries forming perpendicular to the layers. Preferential Bragg peak widening perpendicular to q in diffraction from individual particles corroborates the preferential formation of defects perpendicular to the transition metal-oxide layers. The preferential alignment of dislocations in Na^+ layered oxides is in contrast to interlayer edge dislocations found in Li-ion systems.[3,7] In Li-ion cathodes, Li-ions can migrate to TMO layers. Unlike Li-ions, the Na-ions are larger than transition metal ions and cannot occupy the same crystal sites. The dislocations perpendicular to the layers can therefore serve as escape pathways for Na-ions that cannot migrate to the TMO layers. The formation strain energy of the dislocations is proportional to their length, defined by the particle morphology, and the component of shear modulus along the Burgers vector. Both the edge and screw dislocations with the Burgers vector perpendicular to the layers depend on the same value of an orthotropic shear modulus; hence the ratios of the particle size parallel ($d_{\parallel}$) and perpendicular ($d_{\perp}$) to the layers dictate the preferable dislocation formation. Consequently, in the plate-like morphology of P2-$Na_{0.66}Ni_{0.33}Mn_{0.66}O_2$ and P2-$Na_{0.78}Ni_{0.23}Mn_{0.69}O_2$ particles, screw dislocations normal to the layers are energetically more favorable. Mesostructure in cathodes is known to affect electrochemical performance,[38] and our findings on the role of external stress perpendicular to the layers ([001] direction) in the defect formation process offer a possible mechanism. The morphology effect raises an intriguing possibility to design Na^+ ion battery cathode materials to minimize the number of defects or promote their preferential orientation for controlling the speed of cation and, at high voltage, anion diffusion.

4. Experimental Section

Materials Synthesis: P2-$Na_{0.78}Ni_{0.23}Mn_{0.69}O_2$ was synthesized using a titration technique as described previously.[23] 60 mL of a Na_2CO_3 solution was added dropwise to a 10 mL solution of $Ni(NO_3)_2$ and $Mn(NO_3)_2$ (Ni:Mn = 1:3 molar ratio) where the CO_3:TM ratio was 1:1. The resulting solution was transferred to a 100 mL Teflon-lined stainless steel autoclave and aged at 80 °C for 12 h. The resulting $Ni_{025}Mn_{0.75}CO_3$ particles were mixed with a stoichiometric amount of Na_2CO_3, and the mixture was calcined at 900 °C for 12 h. P2-$Na_{0.66}Ni_{0.33}Mn_{0.66}O_2$ was synthesized using a co-precipitation method. Stoichiometric amounts of precursors, $Ni(NO_3)_2$ and $Mn(NO_3)_2$ (Ni:Mn ratio = 1:2 molar ratio) were dissolved in deionized water for a total concentration of 1 M. The TM nitrate solution and a 0.2 M Na_2CO_3 aqueous solution were pumped separately into a reaction vessel to maintain a pH of 7.8. The obtained mixture was aged at 80 °C for 12 h. The resulting $Ni_{0.33}Mn_{0.66}CO_3$ was washed with deionized water and dried at 80 °C overnight. The $Ni_{0.33}Mn_{0.66}CO_3$ powder was mixed with a 5% excess stoichiometric ratio of Na_2CO_3 and calcined at 900 °C for 12 h.

Electrochemical Tests: Cathode electrodes were prepared by mixing slurry of 80 wt% active material with 10% acetylene black and 10% polyvinylidene fluoride (PVDF) with *N*-methyl-2- pyrrolidone as the solvent. The slurry was cast onto aluminum foil and dried at 80 °C under vacuum overnight. Na metal was used as the counter electrode with 1 M $NaPF_6$ in propylene carbonate (PC) as the electrolyte and GF/F (Whatman) as the separator. Battery assembly was carried out in an MBraun

glovebox (H_2O < 0.1 ppm). Modified in situ CR2032 coin cells were used for CXDI experiments as previously described.[3] The cells were charged from open circuit voltage value up to 4.5 V versus Na^+/Na at a current rate of C/10.

Experimental Details: The BCDI experiments were conducted at the 34 ID-C beamline of the Advanced Photon Source (Argonne National Laboratory, ANL, USA). The cells were mounted on standard sample holders manufactured using a 3D printer. A photon energy of 9 keV and sample-to-detector distances from 60 cm to 2 m were used in the experiments. Timepix (34ID) 2D detector with a pixel size of 55 μm × 55 μm was used.

X-Ray Data Collection and Reconstruction Procedure: In all experiments rocking scans around a 002 Bragg peak, ≈1° wide with 50–100 points and 0.5–2 second exposure, were collected. Before the operando measurement, 10–20 particles were chosen for tracking in each coin cell. During the operando measurement, the chosen particles were measured in sequence, leading to a time step of 30 min between measurements of the same particles. The scheme of the experiment and an example of individual diffraction patterns can be found in Figure S7, Supporting Information: BCDI scheme. During the analysis, the reconstruction procedure combined error-reduction (ER) alternating with hybrid input–output (HIO) algorithm. The diffraction data were binned by 2 along both dimensions of the detector before running reconstructions. Reconstruction without binning was also tested but produced worse results. Different iteration numbers between 410 and 1000 were attempted, with the final number settled at 610. All attempts resulted in very similar reconstructions. An average of 5 results was used in this work, each being an average of 20 best reconstructions retrieved in a guided procedure developed in Ref. [6] (8 generations, 40 population). The errors in Figures 4 and 5 are calculated as a standard deviation between different reconstructions. The nanoparticle shape was found by averaging the amplitudes of the reconstructions at different voltages, assuming the nanoparticle shape change during charge is negligible, and applying a threshold of 10% to that average amplitude (see also Ref. [5]). The reconstructions were run using a GPU optimized code on multiple GeForce 1080 and 2080 graphics cards.

Supporting Information

Supporting Information is available from the Wiley Online Library or from the author.

Conflict of Interest

The authors declare no conflict of interest.

Author Contributions

O.Yu.G., H.H., D.S., D.W., R.B., Z.W., W.C., J.M, R.H., and A.S. conducted the coherent X-ray measurements; H.H., M.Z. and Y.S.M. synthesized the cathode materials, performed the scanning electron microscopy and assembled the batteries; O.Yu.G. performed data reduction, analysis and mechanical interpretation, with contributions from H.H., D.S., S.D.M., Y.S.M. and A.S.; O.Yu.G., H.H., L.H.B.N. and A.S. wrote the paper. All authors contributed to discussions and commented on the manuscript.

**ADVANCED
SCIENCE NEWS**

www.advancedsciencenews.com

**ADVANCED
ENERGY
MATERIALS**

www.advenergymat.de

Data Availability Statement

The data that support the findings of this study are available from the corresponding author upon reasonable request.

Keywords

[1] W. Shockley, *Proc. IRE* **1952**, *40*, 1289.

[2] D. Hull, D. J Bacon, *Introduction to Dislocations*, Butterworth-Heinemann, Oxford, UK **2011**.

[3] A. Singer, M. Zhang, S. Hy, D. Cela, C. Fang, T. A. Wynn, B. Qiu, Y. Xia, Z. Liu, A. Ulvestad, N. Hua, J. Wingert, H. Liu, M. Sprung, A. V. Zozulya, E. Maxey, R. Harder, Y. S. Meng, O. G. Shpyrko, *Nat. Energy* **2018**, *3*, 641.

[4] P. Yan, J. Zheng, M. Gu, J. Xiao, J.-G. Zhang, C.-M. Wang, *Nat. Commun.* **2017**, *8*, 14101.

[5] M. J. Hÿtch, J.-L. Putaux, J.-M. Pénisson, *Nature* **2003**, *423*, 270.

[6] J. Y. Huang, L. Zhong, C. M. Wang, J. P. Sullivan, W. Xu, L. Q. Zhang, S. X. Mao, N. S. Hudak, X. H. Liu, A. Subramanian, H. Fan, L. Qi, A. Kushima, J. Li, *Science* **2010**, *330*, 1515.

[7] Y. Gong, Y. Chen, Q. Zhang, F. Meng, J.-A. Shi, X. Liu, X. Liu, J. Zhang, H. Wang, J. Wang, Q. Yu, Z. Zhang, Q. Xu, R. Xiao, Y.-S. Hu, L. Gu, H. Li, X. Huang, L Chen, *Nat. Commun.* **2018**, *9*, 8.

[8] A. M. Abakumov, A. A. Tsirlin, I. Bakaimi, G. V. Tendeloo, A. Lappas, *Chem. Mater.* **2014**, *26*, 3306.

[9] R. J. Clément, D. S. Middlemiss, I. D. Seymour, A. J. Ilott, C. P. Grey, *Chem. Mater.* **2016**, *28*, 8228.

[10] P.-V. Ong, Z. Yang, P. V. Sushko, Y. Du, *J. Phys. Chem. Lett.* **2018**, *9*, 5515.

[11] J. Zhao, L. Zhao, K. Chihara, S. Okada, J.-i. Yamaki, S. Matsumoto, S. Kuze, K. Nakane, *J. Power Sources* **2013**, *244*, 752.

[12] D. Larcher, J.-M. Tarascon, *Nat. Chem.* **2014**, *7*, 19.

[13] R. J. Clément, P. G. Bruce, C. P. Grey, *J. Electrochem. Soc.* **2015**, *162*, A2589.

[14] N. Yabuuchi, K. Kubota, M. Dahbi, S. Komaba, *Chem. Rev.* **2014**, *114*, 11636.

[15] C. P. Grey, J. M. Tarascon, *Nat. Mater.* **2016**, *16*, 45.

[16] J. Woods, N. Bhattarai, P. Chapagain, Y. Yang, S. Neupane, *Nano Energy* **2019**, *56*, 619.

[17] A. J. Merryweather, C. Schnedermann, Q. Jacquet, C. P. Grey, A. Rao, *Nature* **2021**, *594*, 522.

[18] A. Senyshyn, M. J. Mühlbauer, K. Nikolowski, T. Pirling, H. Ehrenberg, *J. Power Sources* **2012**, *203*, 126.

[19] A. Ulvestad, A. Singer, J. N. Clark, H. M. Cho, J. W. Kim, R. Harder, J. Maser, Y. S. Meng, O. G Shpyrko, *Science* **2015**, *348*, 1344.

[20] M. Dupraz, G. Beutier, T. W. Cornelius, G. Parry, Z. Ren, S. Labat, M.-I. Richard, G. A. Chahine, O. Kovalenko, M. D. Boissieu, E. Rabkin, M. Verdier, O Thomas, *Nano Lett.* **2017**, *17*, 6696.

[21] J. N. Clark, J. Ihli, A. S. Schenk, Y.-Y. Kim, A. N. Kulak, J. M. Campbell, G. Nisbet, F. C. Meldrum, I. K Robinson, *Nat. Mater.* **2015**, *14*, 780.

[22] A. Ulvestad, J. N. Clark, R. Harder, I. K. Robinson, O. G. Shpyrko, *Nano Lett.* **2015**, *15*, 4066.

[23] C. Ma, J. Alvarado, J. Xu, R. J. Clément, M. Kodur, W. Tong, C. P. Grey, Y. S. Meng, *J. Am. Chem. Soc.* **2017**, *139*, 4835.

[24] R. J. Clément, J. Xu, D. S. Middlemiss, J. Alvarado, C. Ma, Y. S. Meng, C. P. Grey, *J. Mater. Chem. A* **2017**, *5*, 4129.

[25] N. Cai, W. Wei, *Imperfections in Crystalline Solids*, Cambridge University Press, Cambridge **2016**.

[26] J. Godeta, P. Hirel, S. Brochard, L. Pizzagalli, *J. Appl. Phys.* **2009**, *105*, 026104.

[27] H. Yang, J. Xiao, Z. Yao, X. Zhang, F. Younus, R. Melnik, *Diamond Relat. Mater.* **2018**, *88*, 110.

[28] L. Y. Chen, M.-r. He, J. Shin, G. Richter, D. S. Gianola, *Nat. Mater.* **2015**, *14*, 707.

[29] Y. Sun, S. Guo, H. Zhou, *Energy Environ. Sci.* **2019**, *12*, 825.

[30] C. Wang, L. Liu, S. Zhao, Y. Liu, Y. Yang, H. Yu, S. Lee, G.-H. Lee, Y.-M. Kang, R. Liu, F. Li, J. Chen, *Nat. Commun.* **2021**, *12*, 2256.

[31] C. Delmas, D. Carlier, M. Guignard, *Adv. Energy Mater.* **2021**, *11*, 2001201.

[32] P.-F. Wang, Y. You, Y.-X. Yin, Y.-G. Guo, *Adv. Energy Mater* **2018**, *8*, 1701912.

[33] D. A. Cogswell, M. Z. Bazant, *ACS Nano* **2012**, *6*, 2215.

[34] J. Mao, X. Liu, J. Liu, H. Jiang, T. Zhang, G. Shao, G. Ai, W. Mao, Y. Feng, W. Yang, G. Liu, K. Dai, *J. Electrochem. Soc.* **2019**, *166*, A3980.

[35] J. J. Huang, D. Weinstock, H. Hirsh, R. Bouck, M. Zhang, O. Y. Gorobtsov, M. Okamura, R. Harder, W. Cha, J. P. C. Ruff, Y. Shirley Meng, A. Singer, *Adv. Energy Mater.* **2022**, *12*, 2103521.

[36] B. E. Warren, *X-Ray Diffraction.*, Dover Publications Inc., Mineola, NY **1990**.

[37] J. Alvarado, C. Ma, S. Wang, K. Nguyen, M. Kodur, Y. S. Meng, *ACS Appl. Mater. Interfaces* **2017**, *9*, 26518.

[38] H. Hirsh, M. Olguin, H. Chung, Y. Li, S. Bai, D. Feng, D. Wang, M. Zhang, Y. S. Meng, *J. Electrochem. Soc.* **2019**, *166*, A2528.

[39] Z. Lu, J. R. Dahn, *J. Electrochem. Soc.* **2001**, *148*, A1225.

[40] S. Lou, Q. Liu, F. Zhang, Q. Liu, Z. Yu, T. Mu, Y. Zhao, J. Borovilas, Y. Chen, M. Ge, X. Xiao, W.-K. Lee, G. Yin, Y. Yang, *Nat. Commun.* **2020**, *11*, 5700.